Engineering Geology 211 (2016) 135–149

Contents lists available at ScienceDirect

Engineering Geology

journal homepage: www.elsevier.com/locate/enggeo

Probabilistic and spatial assessment of liquefaction-induced settlements through multiscale random field models

Qiushi Chen [a], Chaofeng Wang [a], C. Hsein Juang [b,a,*]

[a] Glenn Department of Civil Engineering, Clemson University, Clemson, SC 29634, USA
[b] College of Transportation Engineering, Tongji University, Shanghai 200092, China

ARTICLE INFO

Article history:
Received 7 March 2016
Received in revised form 1 July 2016
Accepted 4 July 2016
Available online xxxx

Keywords:
Liquefaction settlement
Cone penetration test (CPT)
Spatial variability
Probabilistic analysis
Random field model

ABSTRACT

Evaluation of liquefaction-induced settlements over an extended area requires the integration of different solution models that can account for the liquefaction resistance of a given soil profile and its spatial dependence across scales. In this paper, a CPT-based liquefaction model is adopted to estimate the liquefaction-induced settlement at individual sounding locations. The model is then integrated with multiscale random field models to account for spatial variability of soil properties. One important advantage of the proposed framework is its ability to consistently refine and provide settlement estimations across different scales, from regional and geologic unit scales down to a local, site-specific scale. The proposed methodology is then applied to the Alameda County, California, an earthquake-prone region, to illustrate the procedure for probabilistic and spatial assessment of liquefaction-induced settlements at different scales.

1. Introduction

Assessment and mitigation of regional liquefaction hazard require a reliable tool for evaluating not only the probability of liquefaction occurrence, but also, more importantly, the associated effects within a region. Ground surface settlements due to soil liquefaction have been one of the major causes for infrastructure damages during an earthquake. Evaluation of liquefaction-induced settlement at individual locations, where field tests such as the cone penetration test (CPT) are performed, can be achieved through classical empirical liquefaction models. To map liquefaction settlement over an extended area, however, the spatial dependence of soil properties across the region must be taken into account. This paper presents a framework for integrating the classical liquefaction models (e.g., a CPT-based liquefaction-induced settlement model) and tools from geostatistics (e.g., multiscale random field models) for the probabilistic and spatial assessment of liquefaction-induced settlements across an earthquake-prone region, from regional and geologic unit scales down to a local, site-specific scale.

1.1. Previous work

Evaluation and prediction of liquefaction-induced settlement have been the subject of intensive research for the past several decades. Among various approaches, use of empirical relationships based on the correlation of observed soil behavior with various in-situ index tests or laboratory tests remains the dominant approach for assessing liquefaction-induced settlement, e.g., (Lee and Albaisa, 1974; Tokimatsu and Seed, 1984, 1987; Nagase and Ishihara, 1988; Ishihara and Yoshimine, 1992; Pradel, 1998; Shamoto et al., 1998; Zhang et al., 2002; Wu and Seed, 2004; Tsukamoto et al., 2004; Lee, 2007; Cetin et al., 2009a, 2009b; Lu et al., 2009; Ueng et al., 2010; Tsukamoto and Ishihara, 2010; Juang et al., 2013; Valverde-Palacios et al., 2014). In particular, using cone penetration test (CPT) data, Zhang et al. (2002) proposed a method that couples the volumetric strain chart by Ishihara and Yoshimine (1992) to the classical CPT-based liquefaction model by Robertson and Wride (1998) for evaluation of liquefaction-induced settlements. Building on the work of Zhang et al. (2002) and Juang et al. (2013) proposed a probabilistic approach to estimate probability of exceeding a settlement threshold. Using laboratory data and empirical correlations, probabilistic models were developed in Cetin et al. (2009a,b) for cyclic volumetric and shear strains, which were correlated to typical field index test results such as the corrected standard penetration test blow counts or the cone penetration test tip resistance, to predict field settlements.

All of the aforementioned work estimates the liquefaction-induced settlement, or the probability of exceeding a particular settlement threshold, at individual locations. To assess the consequences of liquefaction over extended areas or to map the estimated liquefaction settlements to a region, it is necessary to account for the spatial dependence of soil properties and/or the predicted settlements. Tools developed in geostatistics have received considerable attention in recent years and have been applied to assess liquefaction hazard over large regions. For

* Corresponding author at: Glenn Department of Civil Engineering, Clemson University, Clemson, SC 29634, USA.
E-mail address: hsein@clemson.edu (C.H. Juang).

http://dx.doi.org/10.1016/j.enggeo.2016.07.002
0013-7952/

instance, Liu and Chen (2006) used CPT measurements to estimate the spatial structure of soil deposits. Then, random field models were coupled with Monte Carlo simulations to assess liquefaction potential in the Yuanlin area of Taiwan. Vivek and Raychowdhury (2014) explicitly considered the spatial variations of soil indices from CPT soundings when evaluating liquefaction potential. It has been found that the probability of liquefaction could be significantly underestimated if the spatial dependence of soil indices has not been considered. Chen et al. (2015) developed a random field-based approach to map liquefaction potentials across scales, where the spatial variability of the Liquefaction Potential Index (LPI) developed by Iwasaki et al. (1978, 1982)) is explicitly considered through internally-consistent probabilistic models developed at multiple scales. LPI has also been adopted and modified to assess liquefaction potentials at individual CPT soundings or over extended region (Sonmez, 2003; Sonmez and Gokceoglu, 2005; Papathanassiou et al., 2005; Holzer et al., 2006; Baise et al., 2006; Lenz and Baise, 2007; Thompson et al., 2007; Juang et al., 2008b). In another recent work by van Ballegooy et al. (2015), four liquefaction vulnerability parameters, including the LPI, were used to map liquefaction hazards in the Christchurch area using an extensive CPT database. In contrast to the substantial efforts incorporating geostatistics tools into liquefaction potential evaluation, relatively few studies have addressed liquefaction-induced settlement over an extended area. In Hinckley (2010) and Bartlett et al. (2007), the classical methods of Tokimatsu and Seed (1987), Ishihara and Yoshimine (1992), Bartlett and Youd (1995), Youd et al. (2002) and Yoshimine et al. (2006) are employed to calculate liquefaction-induced lateral spread and ground settlement, which are plotted within their respective surficial geologic units. Each geologic unit is then assigned an estimate of ground deformation based on statistical analysis.

In this work, a CPT-based liquefaction model is coupled with novel geostatistics tools for the probabilistic and spatial assessment of the liquefaction-induced settlements over a region and across different scales. The remainder of the paper is structured as follows: in Section 2, the classical Robertson and Wride 1998 CPT-based liquefaction model is briefly presented, which will be used to evaluate the liquefaction-induced settlement in Section 3. In Section 4, multiscale random field models are developed to map the liquefaction settlement over the region of interest. The proposed framework is then applied to analyze liquefaction settlement hazards in an earthquake-prone region, i.e., the Alameda County of California, in Section 5 followed by some concluding remarks in Section 6.

2. The updated Robertson and Wride 1998 CPT-based liquefaction model

The CPT-based liquefaction model proposed by Robertson and Wride (1998) and subsequently updated by Robertson (2009) is adopted in this work to evaluate the liquefaction resistance of sandy soils. The main elements of this classical procedure are briefly summarized in this section. The evaluation involves the use of two variables: the capacity of the soil to resist liquefaction, expressed in terms of the cyclic resistance ratio (CRR); and the seismic demand on a soil layer placed by a given earthquake, expressed in terms of the cyclic stress ratio (CSR). If the estimated CSR is greater than CRR, the soil is said to liquefy during the given earthquake.

The cyclic resistance ratio (CRR) is estimated as

$$\mathrm{CRR} = \begin{cases} 0.8333\left[(q_{c1N})_{cs}/1000\right] + 0.05 & \text{if} \quad (q_{c1N})_{cs} < 50 \\ 93\left[(q_{c1N})_{cs}/1000\right]^3 + 0.08 & \text{if} \quad 50 \le (q_{c1N})_{cs} < 160 \end{cases} \tag{1}$$

The equivalent clean sand normalized penetraction resistance, denoted as $(q_{c1N})_{cs}$, is given as

$$(q_{c1N})_{cs} = K_c (q_{c1N}) \tag{2}$$

where the conversion factor K_c for grain characteristics is calculated from the soil behavior type index I_c as

$$Kc = \begin{cases} 1 & \text{for} \quad I_c \le 1.64 \\ -0.403 I_c^4 + 5.581 I_c^3 - 21.63 I_c^2 + 33.75 I_c - 17.88 & \text{for} \quad I_c > 1.64 \end{cases} \tag{3}$$

and q_{c1N} is the normalized cone penetration resistance calculated as

$$q_{c1N} = \left(\frac{q_c - \sigma_{vo}}{P_{at}}\right)\left(\frac{P_{at}}{\sigma'_{vo}}\right)^n \tag{4}$$

where $P_{at} = 1$ atm of pressure (100 kPa); P_{at}/σ'_{vo} should not exceed a value of 1.7 as specified by Youd et al. (2001); q_c is the measured cone penetration resistance; n is the stress exponent, given by

$$n = 0.381(I_c) + 0.05\left(\frac{\sigma'_{vo}}{P_{at}}\right) - 0.15 \quad \text{where} \quad n \le 1. \tag{5}$$

The soil behavior type index, I_c, is defined by Robertson and Wride (1998) as

$$I_c = \sqrt{(3.47 - \log Q)^2 + (1.22 + \log F)^2} \tag{6}$$

where Q and F are the normalized tip resistance and friction ratio, respectively.

$$Q = \left(\frac{q_c - \sigma_{vo}}{\sigma'_{vo}}\right) \tag{7}$$

$$F = \left(\frac{f_s}{q_c - \sigma_{vo}}\right) \times 100\% \tag{8}$$

For the cyclic stress ratio (CSR), the following adjusted form is used

$$\mathrm{CSR} = 0.65\left(\frac{a_{\max}}{g}\right)\left(\frac{\sigma_{vo}}{\sigma'_{vo}}\right)(r_d)\left(\frac{1}{\mathrm{MSF}}\right)\left(\frac{1}{K_\sigma}\right) \tag{9}$$

where $a_{\max}$ is the peak horizontal acceleration at the ground surface generated by a given earthquake; g is the gravitational acceleration; σ_{vo} and σ'_{vo} are the total and effective vertical overburden stresses, respectively; r_d is the depth-dependent shear stress reduction coefficient; MSF is the magnitude scaling factor; K_σ is the overburden correction factor for the cyclic stress ratio ($K_\sigma = 1$ for $\sigma'_{vo} < 1$ atm (1 atm = 100 kPa)). The stress reduction factor, r_d, is estimated based on the recommendation by Youd et al. (2001), which takes the following form

$$r_d = \frac{1.0 - 0.4113z^{0.5} + 0.04052z + 0.001753z^{1.5}}{1.0 - 0.4177z^{0.5} + 0.05729z - 0.006205z^{1.5} + 0.001210z^2}. \tag{10}$$

The magnitude scaling factor MSF also follows the recommendation in Youd et al. (2001) as

$$\mathrm{MSF} = \frac{10^{2.24}}{M_w^{2.56}} \tag{11}$$

where M_w is the moment magnitude of the earthquake.

Once CSR and CRR are obtained, the factor of safety against liquefaction can be derived

$$\mathrm{FS} = \frac{\mathrm{CRR}}{\mathrm{CSR}}. \tag{12}$$

The above classical liquefaction model expresses the liquefaction potential of a given soil profile in terms of factor of safety. For cases where there is a need to express the liquefaction potential in terms of liquefaction probability, a probabilistic version of the Robertson and Wride

method is developed by Ku et al. (2012) that links the factor of safety (FS) to the liquefaction probability (P_L), expressed as

$$P_L = 1-\Phi\left[\frac{0.102 + \ln(\mathrm{FS})}{0.276}\right] \approx \left[\frac{1}{1+(\mathrm{FS}/0.9)^6}\right] \tag{13}$$

where Φ is the standard normal cumulative distribution function. It should be noted that the above relation is specific to the Robertson and Wride (1998) model; therefore, the factor of safety (FS) must be computed using the Robertson and Wride method. Also, coefficients in the above relation are calibrated against the compiled liquefaction database in Ku et al. (2012) with the assumption that the modeling error of the factor of safety follows a lognormal cumulative distribution function with a constant coefficient of variation.

3. Probabilistic estimation of liquefaction-induced settlement at individual CPT sounding

Building on the classical CPT-based liquefaction model, the liquefaction-induced settlement is approximated as a summation of the product of the volumetric strain in each soil layer that is susceptible to liquefaction and the corresponding layer thickness. For a site with level ground that is far from any free water surface, such an approximation is reasonable since the volumetric strain is approximately equal to the vertical strain. When sloping or nearly free-faced ground is involved in the analysis, the deviatoric- or shearing-induced deformation should be considered when estimating ground settlement. For instance, Wu and Seed (2004) recommended increasing the ground settlement estimation by an amount equal to 10–20% of the observed or estimated lateral ground displacement. If the estimated lateral ground displacement is smaller than 0.3 m, the influence of the deviatoric deformation is insignificant. In this study, we assume the level ground condition for our evaluation, where the predicted liquefaction-induced settlement S is estimated as Juang et al. (2013)

$$S = \sum_{i=1}^{n} \varepsilon_{vi} \Delta z_i \mathrm{IND}_i \tag{14}$$

where ε_{vi} is the volumetric strain of the ith layer; Δz_i is the thickness of the ith layer; IND_i is an indicator of liquefaction occurrence in the ith layer; and n is the total number of layers. In Zhang et al. (2002), IND is taken as 1 for all soil layers. It should be noted that, the adopted Zhang et al. (2002) model has been previously critically evaluated in the literature. For instance, Juang et al. (2013) found that the Zhang et al. (2002) model tends to overestimate the post-liquefaction settlement. A bias factor for the Zhang et al. (2002) model may be calibrated given a compiled liquefaction-induced settlement database to correct the model prediction, as suggested by Juang et al. (2013).

For sand-like soils, the volumetric strain ε_{vi} of the ith layer is a function of the factor of safety of the ith layer, denoted as FS_i, and the clean-sand equivalence of the corrected cone tip resistance, denoted as q_i. Following the previous work of Zhang et al. (2002) and Juang et al. (2013) that coupled the CPT-based method (Robertson and Wride, 1998) with the volumetric strain relationship (Ishihara and Yoshimine, 1992), the volumetric strain can be approximated with the following equation

$$\varepsilon_v(\%) = \begin{cases} 0 & \text{if} \quad \mathrm{FS} \geq 2 \\ \min\left\{\dfrac{a_0 + a_1 \ln(q)}{1/(2-\mathrm{FS}) - [a_2 + a_3 \ln(q)]}, b_0 + b_1 \ln(q) + b_2 \ln(q)^2\right\} & \text{if} \quad 2 \leq 2 - \dfrac{1}{a_2 + a_3 \ln(q)} < \mathrm{FS} < 2 \\ b_0 + b_1 \ln(q) + b_2 \ln(q)^2 & \text{if} \quad \mathrm{FS} \leq 2 - \dfrac{1}{a_2 + a_3 \ln(q)} \end{cases} \tag{15}$$

where q is in kg/cm ^{2}($\approx$100 kPa); the constant fitting parameters are for $q \leq 80$

$$a_0 = 0.1649, \quad a_1 = -0.006047, \quad a_2 = 1.3009, \quad a_3 = -0.1022$$
$$b_0 = 28.45, \quad b_1 = -9.3372, \quad b_2 = 0.7975$$

for $q > 80$

$$a_0 = 0.3773, \quad a_1 = -0.0337, \quad a_2 = 1.5672, \quad a_3 = -0.1833$$
$$b_0 = 28.45, \quad b_1 = -9.3372, \quad b_2 = 0.7975$$

Fig. 1 plots the relation given in Eq. (15) along with the design chart by Ishihara and Yoshimine (1992), where q is the clean-sand equivalence of the corrected cone tip resistance.

It is noted that, in a deterministic analysis, the indicator function IND_i in Eq. (14) is equal to 0 if the ith layer does not liquefy and equal to 1 if the ith layer liquefies. In the case of a probabilistic analysis, IND_i may be treated as a random variable with its expected value $E[IND_i]$ and variance $V[IND_i]$ related to the probability of liquefaction P_{L_i} of the ith layer (Juang et al., 2013). Accounting for model uncertainties, the FS and q in Eq. (15) are now both nominal values calculated from the measurement, not the actual value. As shown by Juang et al. (2013), the nominal values can be estimated from the probability of liquefaction as

$$E[IND_i] = P_{L_i} \tag{16}$$

$$V[IND_i] = P_{L_i}(1-P_{L_i}). \tag{17}$$

The liquefaction probability P_{L_i} of the ith layer may be determined using a $P_L-\mathrm{FS}$ mapping function previously proposed by Ku et al. (2012) as defined in Eq. (13). Then, the probabilistic version of the predicted liquefaction settlement, S, at an individual CPT sounding is characterized by its mean value μ_S and variance σ_S^2 as (Juang et al., 2013)

$$\mu_S = \sum_{i=1}^{n} \varepsilon_{vi} z_i P_{L_i} \partial \tag{18}$$

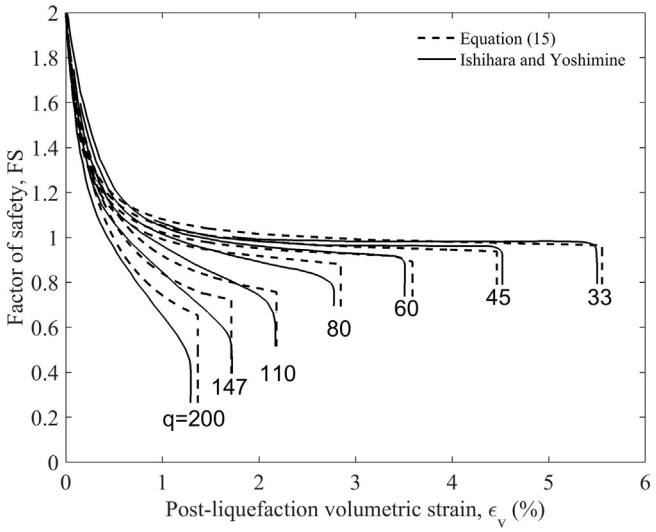

Fig. 1. Chart for estimating the post-liquefaction volumetric strain of clean sand. Adopted from Juang et al. (2013) and Zhang et al. (2002) with the original source data from Ishihara and Yoshimine (1992). Units for the clean-sand equivalence of the corrected cone tip resistance, q, is in kg/cm ^{2}($\approx$100 kPa).

$$\sigma_S^2 = \sum_{i=1}^{n} \varepsilon_{vi}^2 \Delta z_i^2 P_{L_i}(1-P_{L_i}). \tag{19}$$

A further development of the above probabilistic settlement model allows the incorporation and quantification of model error. As suggested by Juang et al. (2013), a multiplicative model bias factor M is introduced and the corrected settlement prediction, denoted as S_a, for a future case can be expressed as

$$S_a = MS = M \sum_{i=1}^{n} \varepsilon_{vi} z_i \mathrm{IND}_i. \tag{20}$$

Assuming that M is independent of S, the mean and variance of the corrected settlement are then given as (Juang et al., 2013)

$$\mu_a = \mu_M \mu_S \tag{21}$$

$$\sigma_a^2 = \mu_M^2 \sigma_S^2 + \sigma_M^2 \mu_S^2 + \sigma_M^2 \sigma_S^2 \tag{22}$$

where μ_M and σ_M are the mean and standard deviation of M; μ_S and σ_S are the mean and standard deviation of the predicted settlement S as defined in Eqs. (18) and (19), respectively. The mean and standard deviation of the model bias factor M may be derived empirically from a database of liquefaction case histories.

4. Characterization of spatial dependence through random field models

The procedure described in Sections 2 and 3 estimates the settlement, either as the nominal value, as in Eq. (20), or as an random variable with mean and variance given in Eqs. (21) and (22). Such estimation is performed at individual CPT sounding locations. To assess the spatial extent of liquefaction damage across a region where the settlement estimations at each location vary, spatial dependence must be considered. In this section, geostatistical tools and multiscale random field models (Baker et al., 2011; Chen et al., 2012, 2015) will be used to characterize spatial dependence and to simulate settlement exceedance at unsampled locations.

4.1. Semivariogram for characterization of spatial dependence

In this study, spatial dependence is described using a form of covariance known as the semivariogram, $\gamma(\mathbf{h})$, which is equal to half the variance of two random variables separated by a vector distance $\mathbf{h}$

$$\gamma(\mathbf{h}) = \frac{1}{2}\mathrm{Var}[Z(\mathbf{u}) - Z(\mathbf{u}+\mathbf{h})] \tag{23}$$

where $Z(\mathbf{u})$ is the variable under consideration as a function of spatial location $\mathbf{u}$; $Z(\mathbf{u}+\mathbf{h})$ is the lagged version of the variable. Sometimes, $Z(\mathbf{u})$ is referred as the "tail" variable; $Z(\mathbf{u}+\mathbf{h})$ is referred as the "head" variable in the geostatistics literature. Under the condition of second-order stationarity (spatially constant mean and variance), the semivariogram is related to other commonly used measures to quantify spatial correlation, i.e., the covariance $COV(\mathbf{h})$ and the correlation $\rho(\mathbf{h})$, as

$$\gamma(\mathbf{h}) = COV(0) - COV(\mathbf{h}) \tag{24}$$

$$\gamma(\mathbf{h}) = COV(0)[1-\rho(\mathbf{h})] \tag{25}$$

where $COV(0)$ is the covariance at $\mathbf{h} = 0$ and equals to the variance σ^2. The semivariogram $\gamma(\mathbf{h})$ is typically preferred by geostatistics community because it only requires the increment $Z(\mathbf{u}) - Z(\mathbf{u}+\mathbf{h})$ to be second-order stationary, i.e., the intrinsic hypothesis, which is a weaker requirement than the second-order stationarity of the variable itself.

It is possible to define a vector $\mathbf{h}$ to account for both separation distance and orientation. The most common approach to modeling the

geometric anisotropy is to define a scalar distance measure as (Isaaks and Srivastava, 1989)

$$h = \sqrt{\left(\frac{h_x}{a_x}\right)^2 + \left(\frac{h_y}{a_y}\right)^2 + \left(\frac{h_z}{a_z}\right)^2} \tag{26}$$

where h_x, h_y and h_z are the scalar component of the vector **h** along the field's principal axes; scalar quantities a_x, a_y and a_z are ranges that specify how quickly spatial dependence decreases along those axes. Characterization and inference of spatial dependence remains a challenging and, to some extent, controversial task. Specific forms of spatial structure adopted in this study will be discussed in more detail in the example application section.

The definition of semivariogram presented above is written in the form of original values of the variables of interest. As pointed out by Gringarten and Deutsch (2001), it is rare in modern geostatistics to consider the untransformed data. The commonly adopted Gaussian simulation technique requires a prior Gaussian transformation of the data. To this end, the inference of the variogram model will be performed on the transformed data, which are obtained by the normal score mapping technique (Goovaerts, 1997). Chen et al. (2012) showed that such transformation does not adversely affect the prescribed spatial structure. Nevertheless, the validity of the correlation should be verified to ensure that the desired spatial dependence relationship is upheld after the transformation.

4.2. Spatial correlation across scales

The previously described spatial correlation has been extended to account for the multiscale nature of soil variability (Chen et al., 2012). This extension allows a higher resolution random field to be adaptively generated around areas of high interest, such as adjacent to critical infrastructures, or around areas of abundant field data. The key of this multiscale extension is to consistently represent fine and coarse scale random fields while maintaining appropriate spatial correlation structures across scales.

In this work, two scales of interest are considered and all subsequent development applies to variables following the standard Gaussian distribution, i.e., variables after a normal score transformation. The derivation of spatial correlation across scales is based on the notion that material properties at the coarser scales are the arithmetically averaged values of the properties over corresponding areas at the finer scales

$$Z_I^c = \frac{1}{N}\sum_{i=1}^{N} Z_{i(I)}^f \tag{27}$$

where superscripts '*c*' and '*f*' correspond to coarse and fine scales, respectively; N = number of fine scale points within a coarse scale area (element) I. Defining the variable of interest at the fine scale and using such a relation, the expression for the variances and spatial correlations of coarse scale variables of interest can be explicitly derived.

The mean of a coarse scale element Z_I^c can be derived by taking the expectation of Eq. (27) as

$$\mu_{Z^c} = E\left[Z_I^c\right] = \frac{1}{N}\sum_{i=1}^{N}\mu_{Z_{i(I)}^f} = 0 \tag{28}$$

where $\mu_{Z_{i(I)}^f}$ is the mean at the fine scale, which is equal to zero for variables following the standard Gaussian distribution. Accordingly, if the variance of the fine scale variable is unity, the coarse scale variance can be computed as

$$\sigma_{Z^c}^2 = E\left[\left(Z_I^c\right)^2\right] - 0 = \frac{1}{N^2}\sum_{i=1}^{N}\sum_{j=1}^{N}\rho_{Z_i^f Z_j^f}\sigma_{Z_i^f}\sigma_{Z_j^f}. \tag{29}$$

The covariance between any two elements Z_i and Z_j within the random field is defined as

$$\mathrm{COV}\left[Z_i, Z_j\right] = \rho_{Z_i Z_j}\sigma_{Z_i}\sigma_{Z_j}. \tag{30}$$

The correlations between all considered scales can be calculated by rearranging the definition of covariance such that

$$\rho_{Z_i Z_j} = \frac{COV\left[Z_i, Z_j\right]}{\sigma_{Z_i}\sigma_{Z_j}} \tag{31}$$

where Z_i and Z_j are two elements within the random field at any scale with variance $\sigma_{Z_i}{}^2$ and $\sigma_{Z_j}{}^2$. By making appropriate substitutions at each scale using Eqs. (30) and (31), the correlation between elements at different scales can be defined as

$$\rho_{Z_I^c Z_{II}^c} = \frac{\sum_{i=1}^{N}\sum_{k=1}^{N}\rho_{Z_{i(I)}^f Z_{k(II)}^f}}{\sqrt{\sum_{i=1}^{N}\sum_{j=1}^{N}\rho_{Z_{i(I)}^f Z_{j(I)}^f}}\sqrt{\sum_{i=1}^{N}\sum_{j=1}^{N}\rho_{Z_{i(II)}^f Z_{j(II)}^f}}} \tag{32}$$

$$\rho_{Z^f Z_I^c} = \frac{\sum_{i=1}^{N}\rho_{Z^f Z_{i(I)}^f}}{\sqrt{\sum_{i=1}^{N}\sum_{j=1}^{N}\rho_{Z_{i(I)}^f Z_{j(I)}^f}}} \tag{33}$$

where the Roman numerals *I*,*II* … are used for coarse scale element numbers; $\rho_{Z_I^c Z_{II}^c}$ = correlation between two coarse-scale elements *I* and *II*; $\rho_{Z^f Z_I^c}$ = correlation between a fine-scale element and a coarse-scale element *I*; $\rho_{Z_{i(I)}^f Z_{k(II)}^f}$ is the correlation between a fine element *i* and a fine element *k*, which belong to two different coarse scale elements *I* and *II*, respectively. Given correlation between elements at different scales, the corresponding semivariogram can be easily obtained through relation Eq. (25) with $COV(h) = 1$ for a standard Gaussian field.

Given the multiscale spatial dependence specified by the semivariogram and an inferred or assumed probability distribution of a parameter value at a single location, a sequential Gaussian simulation process (Goovaerts, 1997) is implemented in Matlab to generate random field realizations of variables of interest.

5. Case study: Alameda County of California

5.1. Analysis region, engineering geology and field data

In this section, the proposed framework is applied for the probabilistic and spatial assessment of liquefaction-induced settlements across a particular earthquake-prone region, the Alameda County of California. A comprehensive digital database of the engineering geology in Alameda County has been compiled by Helley and Graymer (1997) and briefly summarized by Holzer et al. (2006). As shown in Fig. 2, the area contains five major surficial geologic units: artificial fill, younger San Francisco bay mud, Holocene alluvial fan deposits, Merritt sand and Pleistocene alluvial fan deposits. The surficial geology divides the studied area into three broad northwest-southeast-trending regions. Bedrock is exposed at the surface of the northeast land. The central area, immediately to the southwest of the bedrock, consists of Holocene and Pleistocene alluvial fan deposits. The area next to the central area – southwest of the original natural shoreline – is primarily underlain by artificial fill that rests on younger San Francisco Bay mud.

CPT penetration indicates that the thickness of the artificial fill layer ranges from about 11 m to zero. The average thickness is about 3 m. In the central area, the Holocene alluvial fan deposits, which overlap the deposits of Pleistocene age, generally consist of fine grained deposits. This layer was active until modern urban development covered the land surface and channelized the modern streams (Sowers and Richard, 2010). The thickness of the fan deposits ranges from about 14.3 m to zero. The average thickness is about 4.4 m. Beneath the

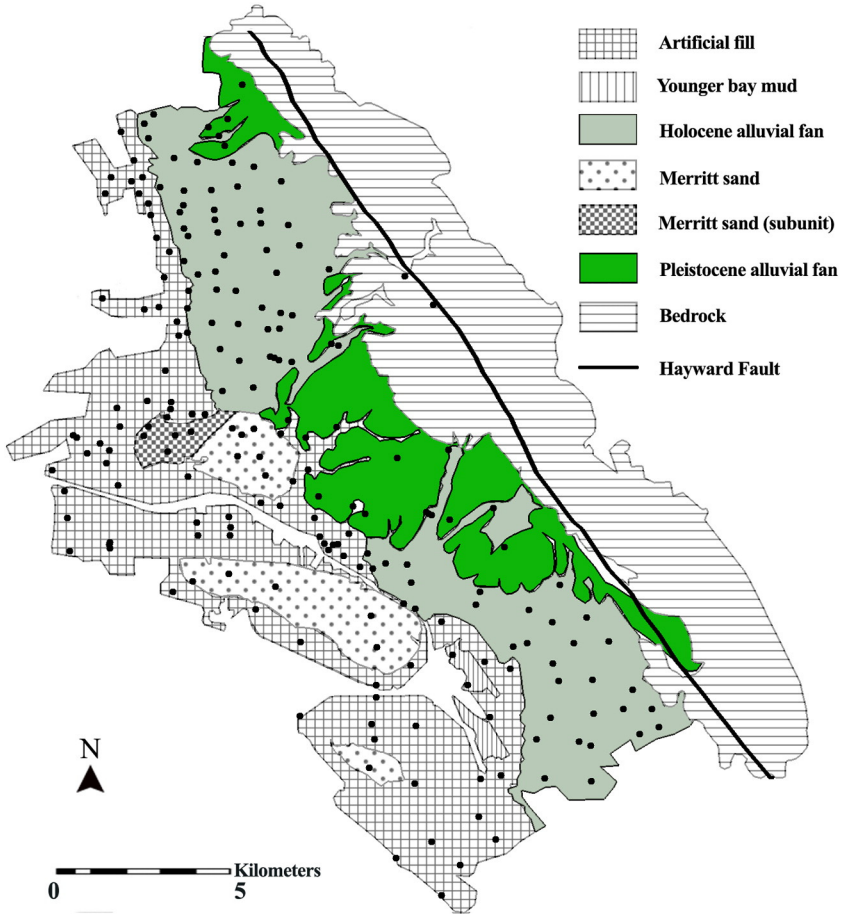

Fig. 2. Site map of the study area (Alameda, Berkeley, Emeryville, Oakland, and Piedmont, California) and locations of CPT soundings (modified from Holzer et al., 2006).

Holocene alluvial fan deposits are the older Pleistocene alluvial fan deposits that were last active during the previous interglacial period (Trask and Rolston, 1951). The wind-blown Merritt sand deposits, resting on the Pleistocene alluvial fan deposits, were chiefly deposited near the end of the Pleistocene epoch when the sea level was lower than it is currently. The ground water table is found to be at 3 m or less below the ground surface in much of the studied area.

Alameda County is a seismically active region at the boundary of the Pacific Plate and the North American Plate. The most important seismic source is the Hayward Fault system (Holzer et al., 2006), as shown in Fig. 2. Additionally, the San Andreas Fault, which stretches roughly 1300 km through California, lies to the west of this region. Herein, the chosen seismic source for the liquefaction analysis is from a hypothetical rupture of the Hayward Fault system. The report by the Working Group on California Earthquake Probabilities (WGCEP) (WGCEP, 2003) predicted the probability in a 30 year period (2002–2031) of one or more earthquakes with magnitude $M_w \geq 6.7$ and $M_w \geq 7.0$ for the Hayward–Rodgers Creek Fault system to be 0.27 and 0.11, respectively. It was also predicted that a rupture of the south segment of the Hayward Fault would produce a magnitude $M_w = 6.6$ earthquake and a rupture of the north segment and the Rodgers Creek would produce a magnitude $M_w = 7.1$ earthquake. The last damaging earthquake on the Hayward Fault was an estimated $M_w = 6.8$ earthquake in 1868, when the southern segment ruptured (WGCEP, 2003). In the following analysis, two earthquake events, corresponding to $M_w = 6.6$ and $M_w = 7.1$, will be considered. Previous analysis by Holzer et al. (2006) mapped liquefaction potential index for this region given the above two earthquake events and will be used to compare the results of this study.

The CPT data used in the case study are taken from the U.S. Geological Survey (USGS) Earthquake Hazard Program CPT database (USGS, 2015). A total of 210 CPT soundings are compiled. The water table information is directly obtained from the CPT sounding record wherever it is available (181 out of the 210 CPT soundings compiled have water table measurement). For CPT soundings without such information, the water table is interpolated. For unit weights of soil, a moist unit weight $\gamma_m = 15.0\ \text{kN}/m^3$ and a saturated unit weight $\gamma_{sat} = 19.4\ \text{kN}/m^3$ are assumed for soils above and below the water table, respectively. Locations of CPT soundings, the surficial geologic units and the outline of the studied region are shown in Fig. 2.

5.2. Deterministic evaluation of liquefaction-induced settlement at CPT soundings

Liquefaction-induced settlement is calculated at each CPT sounding using methodology presented in Section 3 with two hypothetical $M_w = 6.6$ and $M_w = 7.1$ earthquakes on the nearby Hayward Fault. The peak horizontal ground acceleration, $a_{\max}$, is taken as a constant of 0.4 g and 0.5 g for $M_w = 6.6$ and $M_w = 7.1$, respectively. The assumption of a constant $a_{\max}$ is justified on the basis that the outcrop area of each surficial geologic unit is generally parallel and is close to the Hayward Fault (Holzer et al., 2006). Alternatively, at each individual location with known longitude and latitude, the joint distribution of $a_{\max}$ and M_w can be derived using the readily accessible National Seismic Hazard Maps (USGS, 2014) and can be used in conjunction with any liquefaction model. A simplified process incorporating joint distribution of $a_{\max}$ and M_w has been developed in Juang et al. (2008a) and will be considered in a future study.

Histograms of predicted settlements at CPT soundings for the above two earthquake events are shown in Fig. 3.

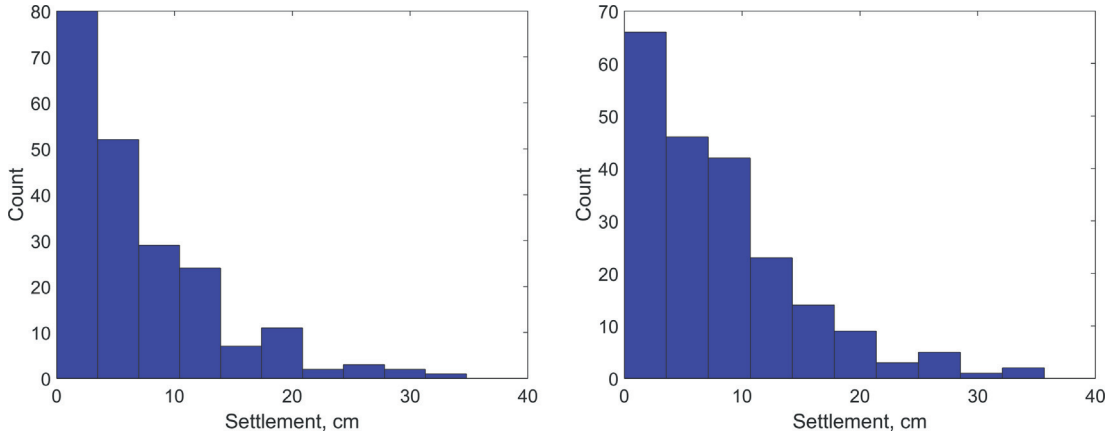

Fig. 3. Histogram of liquefaction-induced settlements at 210 CPT soundings in the Alameda County.

Cumulative frequency functions (CDFs) of predicted settlements at CPT soundings for the above two earthquake events are shown in Fig. 4. The CDF is used to transform the settlements into a Gaussian distribution, upon which the random field simulations run. The transformation is performed as $X' = \Phi^{-1}(F(X))$, where X is the settlement, $F(X)$ is the corresponding CDF, X' is the mapped settlement in Gaussian distribution and Φ is the corresponding CDF in Gaussian distribution.

The liquefaction-induced settlements can be correlated to the extent of the observed damage, and one such correlation was proposed by Ishihara and Yoshimine (1992), shown in the following table.

To estimate the hazard of liquefaction-induced settlement posed by each geologic unit, settlement values at CPT soundings were grouped by surficial geologic unit. Cumulative frequency distributions of settlements are plotted in Fig. 5(a) for $M_w = 6.6$ earthquake and in Fig. 6(a) for $M_w = 7.1$ earthquake. In a previous analysis by Holzer et al. (2006), liquefaction potential index (LPI) were grouped by each geologic unit and used as basis to assess liquefaction hazards posed by each geologic unit. Cumulative frequency distributions of LPIs from Holzer et al. (2006) are shown in Fig. 5(b) for $M_w = 6.6$ earthquake and Fig. 6(b) for $M_w = 7.1$ earthquake for comparison with the current study.

The information presented in Figs. 5 and 6 can be used as an initial quantitative evaluation of liquefaction-induced settlements and the associated extent of damage (ref. Table 1) in each geologic unit. The percentage of soundings underlain by a geologic unit that falls within a certain settlement range may be used as an indication of the approximate percentage of the surface area exhibiting the corresponding damage level. The more CPT soundings included, the better such an approximation becomes.

Following such an interpretation, Fig. 5(a) predicts that, for an $M_w = 6.6$ earthquake event caused by the rupture of the south segment of the Hayward Fault, 42% of the areas underlain by the artificial fill will exhibit medium to extensive damage, which is 21% less than an $Mw = 7.1$ earthquake (Fig. 5(a)). Approximately 13% of the areas underlain by the Holocene alluvial fan will exhibit medium to extensive damage.

For an $M_w = 7.1$ earthquake event, Fig. 6(a) indicates that approximately 53% and 15% of the areas underlain by the artificial fill and the Holocene alluvial fan, respectively, will exhibit medium to extensive damage. Medium to extensive damage is not anticipated for the areas underlain by most of the Pleistocene alluvial fan deposits since only one of the ten CPT soundings in this geologic unit is predicted to have medium damage. This site (numbered as OAK024 in the USGS database (USGS, 2015) and located at 37.792°−122.252° is underlain by the Bull Lake till, which is a softer subunit of Pleistocene fan deposits. Most of the Merritt sand are not anticipated to experience extensive damage either.

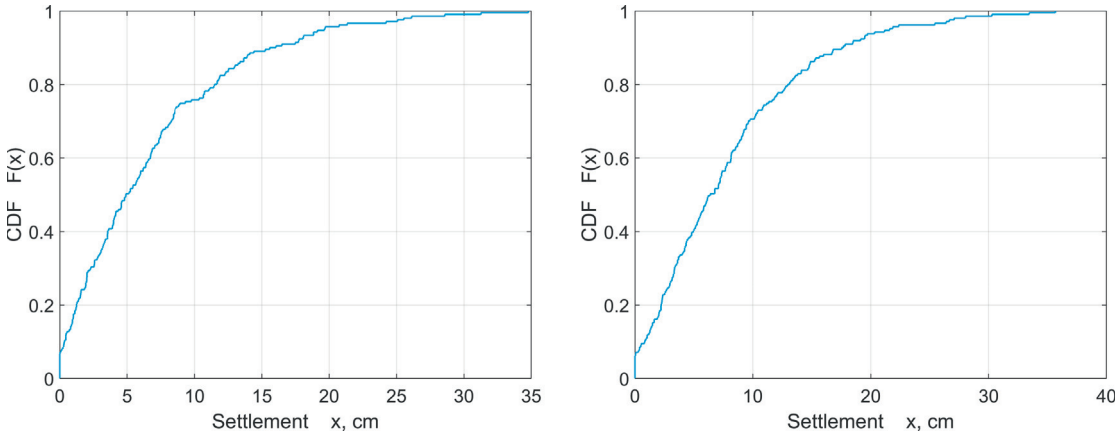

Fig. 4. Cumulative frequency functions of liquefaction-induced settlements at 210 CPT soundings in Alameda County.

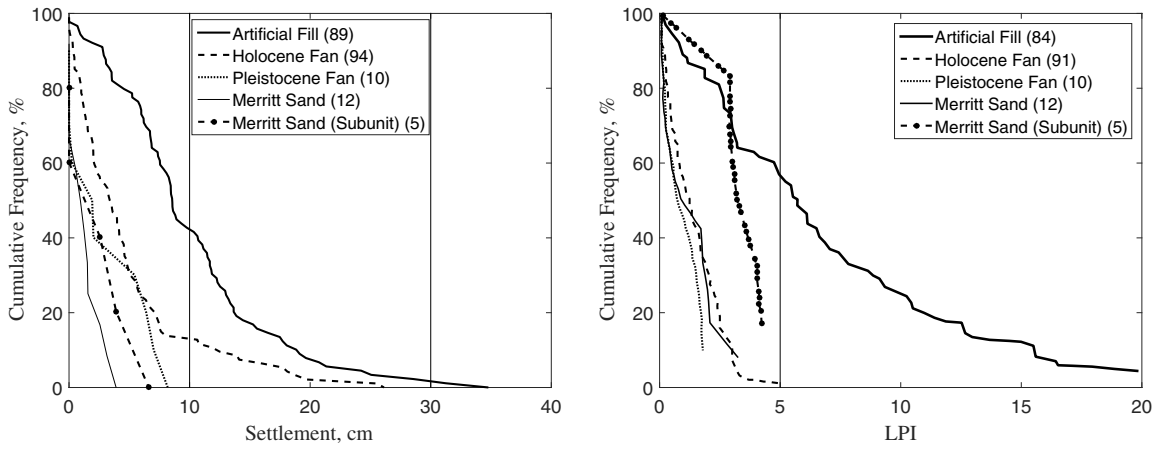

a) Liquefaction-induced settlements b) LPI (adopted from (Holzer et al.,2006))

Fig. 5. Cumulative frequency distributions of liquefaction hazards for an $M_w = 6.6$ earthquake in Alameda County grouped by surficial geologic units. Number of CPT soundings in each geologic unit is shown in parentheses. (a) Liquefaction-induced settlements (b) LPI (adopted from Holzer et al., 2006)

Similarly, based on the calibration of LPI with surface manifestations of liquefaction, it is postulated in Toprak and Holzer (2003) and Holzer et al. (2006) that surface manifestations of liquefaction in general occur when LPI > 5. Fig. 5(b) indicates that, for an $M_w = 6.6$ earthquake event, only the artificial fill will exhibit surface manifestations of liquefaction and 56% of the area underlain by the fill will be affected (LPI > 5), which is 23% less than an $M_w = 7.1$ earthquake event, shown in Fig. 6(b). This is consistent with results obtained using liquefaction-induced settlement (21% difference in predicted damage between the $M_w = 6.6$ and $M_w = 7.1$ events). For an $M_w = 7.1$ earthquake event, Fig. 6(b) indicates that 73% and 3%, respectively, of the areas underlain by the artificial fill and Holocene alluvial fan will exhibit surface manifestations of liquefaction.

It is worth pointing out that, though higher LPI values generally correspond to larger predicted settlements, there is no simple linear relation or one-to-one transformation between those two indices. A surface manifestation of liquefaction (LPI > 5) does not necessarily correspond to medium to extensive damage (settlement > 10 cm). The resemblance of the trends of the cumulative frequency distribution shown in Figs. 5(a) and 6(a) for settlements to that in Figs. 5(b) and 6(b) for LPIs, however, is expected considering the positive correlation between LPI and settlement.

Table 1
Damage extent and approximate settlement (Ishihara and Yoshimine, 1992).

Extent of damage	Settlement (cm)	Phenomena on the ground surface
Light to no damage	0–10	Minor cracks
Medium damage	10–30	Small cracks, oozing of sand
Extensive damage	30–70	Large cracks, spouting of sands large offsets, lateral movement

A closer look into Figs. 5 and 6 reveals significant discrepancy between settlement prediction and LPI prediction for the subunit of Merritt sand deposits, the location of which is shown in Fig. 2. This subunit is identified as the area with higher liquefaction potential, approximately 38% of this subunit is predicted to exhibit liquefaction effects (LPI > 5) in Holzer et al. (2006). However, two of the five CPT soundings within this subarea do not encounter the water table until the end of the penetration. In this study, those two CPT soundings will predict no liquefaction, corresponding to zero LPI or settlement values. Hence, in Figs. 5(a) and 6(a), the cumulative frequency curves for the Merritt sand subunit do not start from 100% and the percentage of this subunit being subjected to liquefaction damage is significantly less than that predicted in (Holzer et al., 2006).

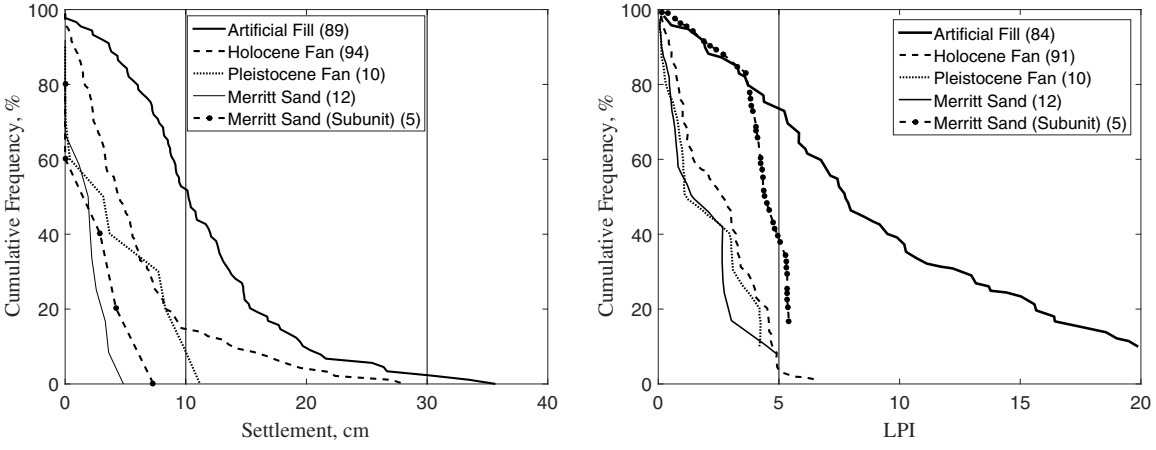

a) Liquefaction-induced settlements b) LPI (adopted from (Holzer et al.,2006))

Fig. 6. Cumulative frequency distributions of liquefaction hazards for an $M_w = 7.1$ earthquake in Alameda County grouped by surficial geologic units. Number of CPT soundings in each geologic unit is shown in the parentheses. (a) Liquefaction-induced settlements (b) LPI (adopted from Holzer et al., 2006)

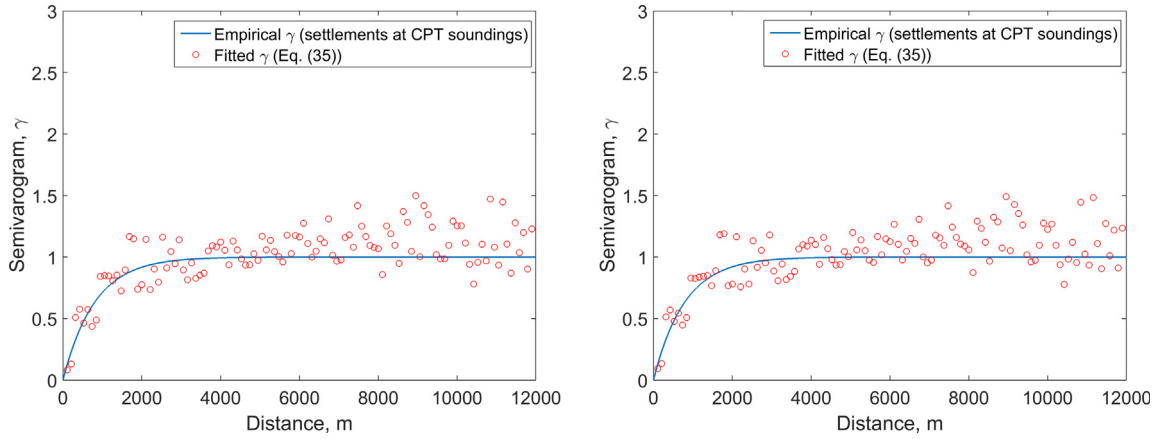

Fig. 7. Empirical and fitted semivariograms of liquefaction-induced settlements at CPT soundings in Alameda County (calculated with lag separate h = 105 m and 20% tolerance). (a) M_w = 6.6 earthquake (b) M_w = 7.1 earthquake.

5.3. Spatial analysis and mapping of liquefaction-induced settlements

Previous analysis focuses on the liquefaction-induced settlements at individual CPT soundings. The probabilistic and cumulative frequency plots are based on information at those isolated locations. To estimate the extent of the liquefaction-induced settlements over a large region, the spatial correlation needs to be considered. In this section, the spatial dependence will be characterized through the semivariogram model, described in detail in Section 4.1. Multiscale random field models will then be used to generate realizations of settlements throughout the region.

The spatial structure of the liquefaction-induced settlements will be obtained from semivariogram inference. Given settlement predictions at 210 CPT soundings and their spatial coordinates, the sample semivariogram $\gamma(\mathbf{h})$ is computed as (Goovaerts, 1997)

$$\gamma(\mathbf{h}) = \frac{1}{2N(\mathbf{h})}\sum_{\alpha=1}^{N(\mathbf{h})}[z(\mathbf{u}_\alpha) - z(\mathbf{u}_\alpha + \mathbf{h})]^2 \tag{34}$$

where $N(\mathbf{h})$ is the number of pairs of data z located a vector $\mathbf{h}$ apart (i.e., a lag bin $\mathbf{h}$). In the actual computation, a small tolerance (e.g., 10–20% of the distance $\mathbf{h}$) is usually added to lag bins to accommodate unevenly spaced sample points. Also, it is often convenient to use a scalar distance measure h, as defined in Eq. (26), for the calculation of semivariogram.

Fig. 7 shows the sample semivariogram based on settlements at 210 CPT soundings for both M_w = 6.6 and M_w = 7.1 earthquake events. Given the sample semivariogram, a weighted least square method by Cressie, 1985) is implemented to fit an analytical semivariogram model, shown as solid line in the plot.

As shown in Fig. 7, the empirical semivariograms for M_w = 6.6 and M_w = 7.1 earthquake events are almost identical, indicating a negligible influence of earthquake intensity on the spatial structure of predicted settlements. In this study, a common semivariogram model is fitted using an exponential model of the form

$$\gamma(h) = 1 - \exp\left(-\frac{3h}{a}\right) \tag{35}$$

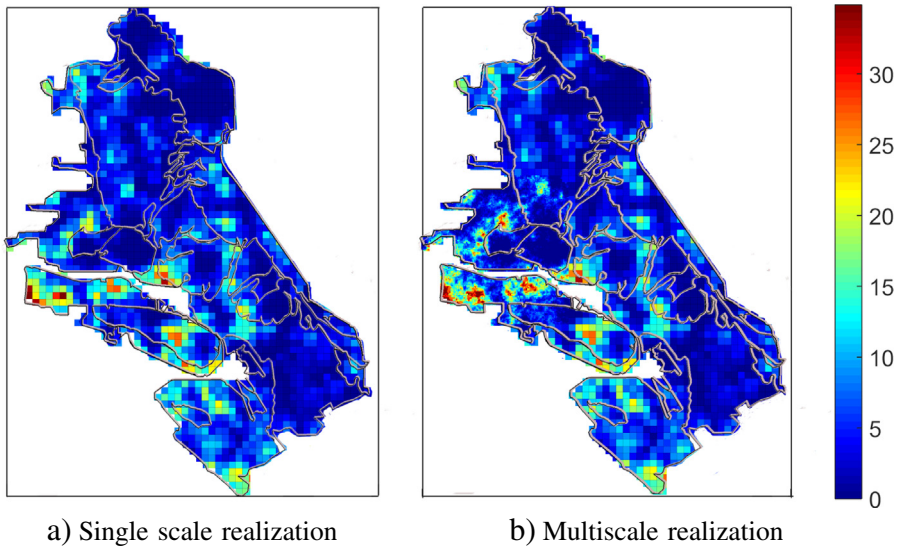

Fig. 8. Typical random field realizations of liquefaction-induced settlements in Alameda County for M_w = 6.6 earthquake event on the Hayward Fault. Unit of the settlement is in cm. Superimposed grey lines correspond to boundaries of geologic units. (a) Single scale realization (b) Multiscale realization.

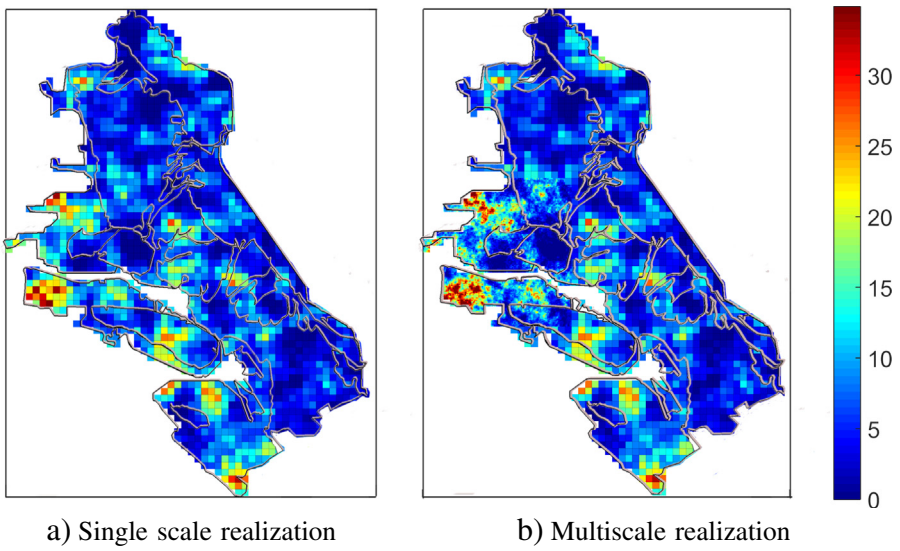

Fig. 9. Typical random field realizations of liquefaction-induced settlements in Alameda County for $M_w = 7.1$ earthquake event on the Hayward Fault. Unit of the settlement is in cm. Superimposed grey lines correspond to boundaries of geologic units. (a) Single scale realization (b) Multiscale realization.

where the practical range $a = 2{,}400$ m. This fitted semivariogram will be used in the random field realization of settlements across the region of interest.

In addition to the semivariogram, the random field model requires the probabilistic distribution of the variable of interest. Herein, a piece-wise linear probability density function is fitted to the histogram of predicted settlements in Fig. 3. A normal score mapping and a sequential Gaussian simulation process are then used to generate random field realizations of variables of interest. Such simulation process has been successfully applied in previous applications and it has been shown that the spatial structure is preserved after normal score mapping and during the simulation process (Baker and Faber, 2008; Baker et al., 2011; Chen et al., 2012, 2015).

Figs. 8 and 9 plot the typical single and multiscale random field realizations of liquefaction-induced settlements for earthquake events $M_w = 6.6$ and $M_w = 7.1$, respectively. In the multiscale realizations, higher resolutions are introduced in the artificial fill geologic unit, where higher liquefaction hazard is expected. It should be noted that, on average, the higher resolution region in a multiscale field resembles the trend seen in the single scale counterpart but with much more detailed information. Such higher resolution information is important when performing local site-specific analysis, as will be shown later.

The corresponding histograms of simulated liquefaction-induced settlements are plotted in Fig. 10. The histograms have preserved the distribution of settlements at 210 CPT locations as previously shown in Fig. 3. Moreover, the spatial structure is also found to be upheld during the simulation.

The random field model can be coupled with Monte Carlo simulations to evaluate various quantities of interest and associated uncertainties. As an example, the cumulative frequency distribution of the predicted settlements are evaluated along with uncertainties in the prediction. Fig. 11 shows the cumulative frequency of the predicted settlements based on a total of 1000 Monte Carlo simulations. The error bar (±one standard deviation) is also included in the cumulative frequency plots. It can be seen that, for the given earthquake events, less than 30% of the Alameda County area is predicted to have a settlement greater

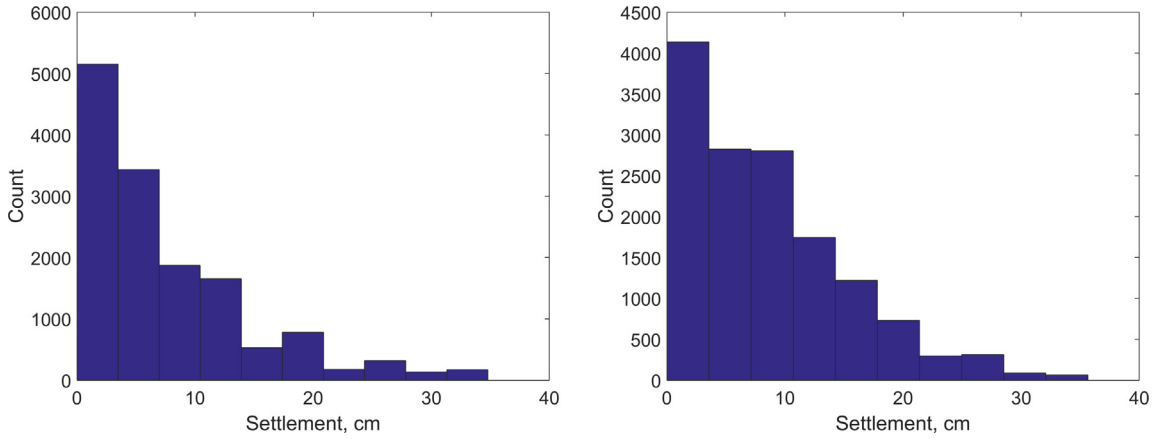

Fig. 10. Typical histograms of simulated liquefaction-induced settlements across the Alameda County. (a) $M_w = 6.6$ earthquake (b) $M_w = 7.1$ earthquake.

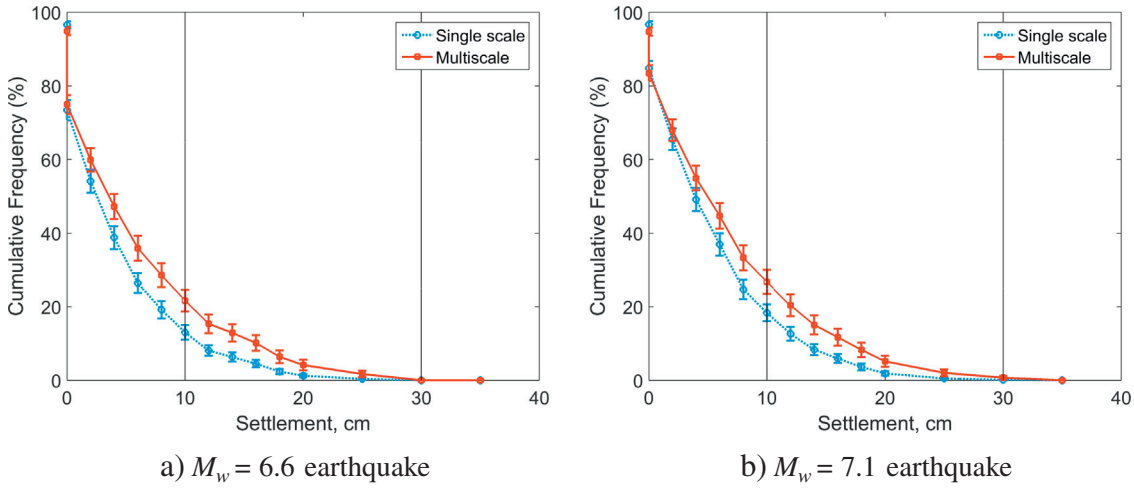

Fig. 11. Cumulative frequency plots of the liquefaction-induced settlements, calculated from 1000 Monte Carlo simulations. (a) $M_w = 6.6$ earthquake (b) $M_w = 7.1$ earthquake.

than 10 cm. The percentage of area predicted to have more than 30 cm settlement is very close to zero. A comparison between the single and multiscale results in Fig. 11 reveals a similar trend but consistently higher predictions with multiscale. For example, for the $M_w = 7.1$ earthquake, the multiscale result indicates that about 27% of the area has a settlement exceeding 10 cm, while the single scale predicts the percentage to be 18%. Since the single (coarse) scale is defined as the average of the corresponding fine scale elements as in Eq. (27), the findings in Fig. 11 indicate that such averaging process might yield an unconservative estimation of liquefaction hazard.

To further demonstrate the capability of random field models and explore their potential applications combined with Monte Carlo simulations, we re-analyze the cumulative frequency distributions of liquefaction-induced settlements grouped by different geologic units, as previously presented in Section 5.2. Instead of using just settlements at CPT soundings, herein, the cumulative frequency distributions are evaluated using settlements throughout Alameda County based on results of 1000 Monte Carlo simulations. The results are summarized in Fig. 12 for both $M_w = 6.6$ and $M_w = 7.1$ earthquake events.

For $M_w = 6.6$ earthquake, Fig. 12(a) indicates that 48.2% of the areas underlain by artificial fill and 7.4% of the areas underlain by Holocene alluvial fan will exhibit medium to extensive damage (settlement greater than 10 cm). The combined region underlain by Merritt sand Pleistocene fan and the northeast portion of the Holocene fan is predicted to have 10% of its area exhibiting medium damage. Only 1% of the subarea underlain by Merritt sand has a medium damage prediction. These predictions are consistent with those made in Section 5.2.

For $M_w = 7.1$ earthquake, Fig. 12(b) indicates that 57.7% and 13.2% , respectively, of the areas underlain by artificial fill and Holocene alluvial fan will exhibit medium to extensive damage. These predictions are very close to the results in Section 5.2, which is 53% and 15%. The combined region underlain by Merritt sand, Pleistocene fan (also including the northeast portion of the Holocene fan) is predicted to have less than 2.4% of its area exhibiting medium damage, which is negligible and again, consistent with predictions made in Section 5.2.

A visualization of the predicted liquefaction-induced settlement mapping, averaged from 1000 Monte Carlo simulations, is shown in Fig. 13(a) along with the LPI mapping obtained from Holzer et al. (2006) shown in Fig. 13(b) for $M_w = 7.1$ earthquake event. As shown in Fig. 13(a), higher settlements (greater than 10 cm) occurs mainly in the southwest region of the original natural shoreline, which is

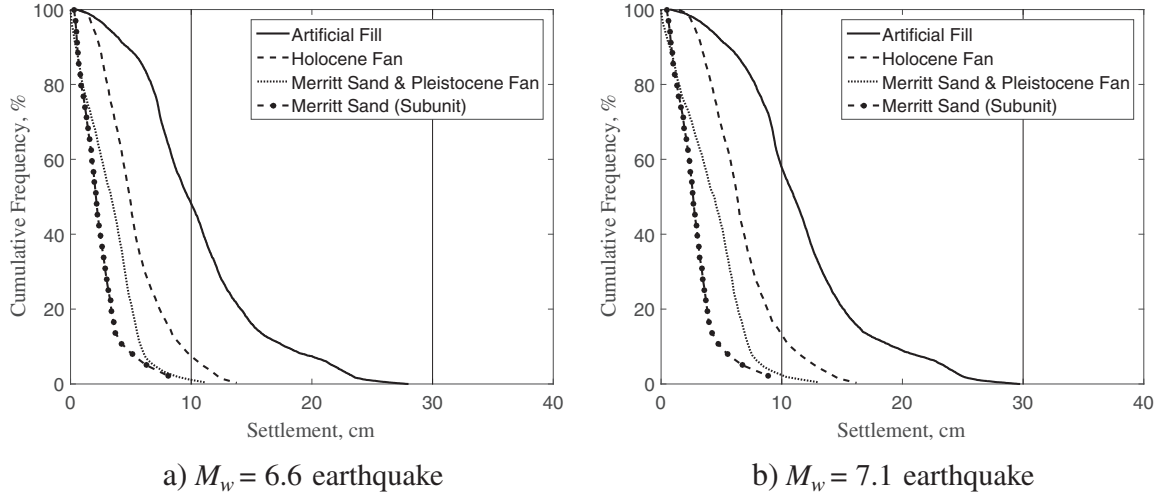

Fig. 12. Cumulative frequency distributions of predicted liquefaction-induced settlements across Alameda County, grouped by surficial geologic units for $M_w = 6.6$ and $M_w = 7.1$ earthquakes on the Hayward Fault. (a) $M_w = 6.6$ earthquake (b) $M_w = 7.1$ earthquake.

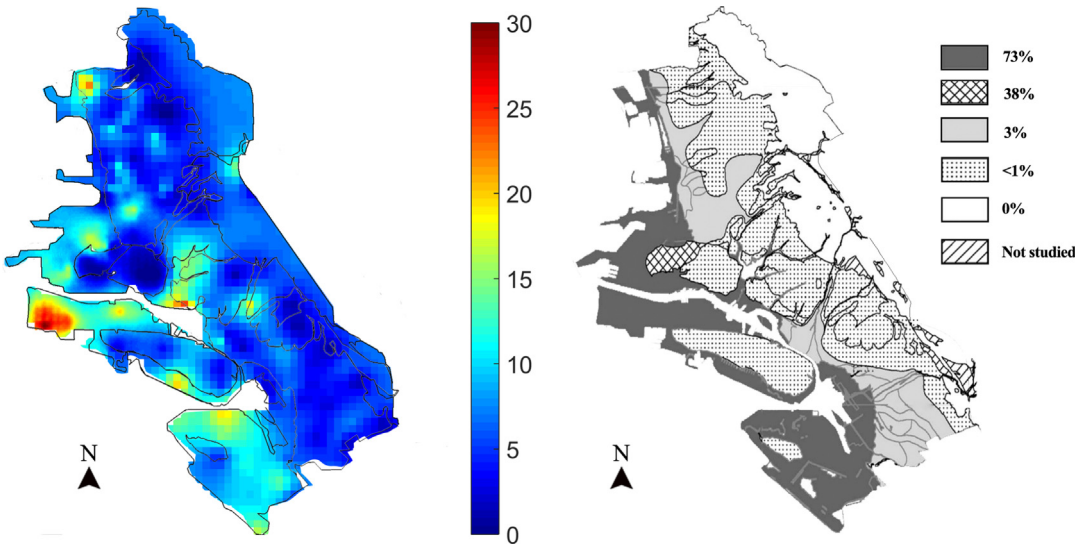

a) Liquefacion-induced settlement mapping

b) Percentage of area predicted to liquefy by LPI (Holzer et al.,2006)

Fig. 13. Liquefaction hazard mapping in the Alameda county site for earthquake event $M_w = 7.1$ on the Hayward Fault. (a) Liquefacion-induced settlement mapping (b) Percentage of area predicted to liquefy by LPI (Holzer et al., 2006).

primarily underlain by the artificial fill that rests on younger San Francisco Bay mud. Similar predictions are made by Holzer et al. (2006) in Fig. 13(b), where there is 73% possibility for this region to exhibit liquefaction. Fig. 13(a) shows that the region close to the northeast of the shoreline, which is underlain by Holocene fan deposits, is predicted to experience minor settlements (most of the values do not exceed 10 cm). To the northeast of the Holocene fan, the combined region including a portion of Alameda island, is not anticipated to experience

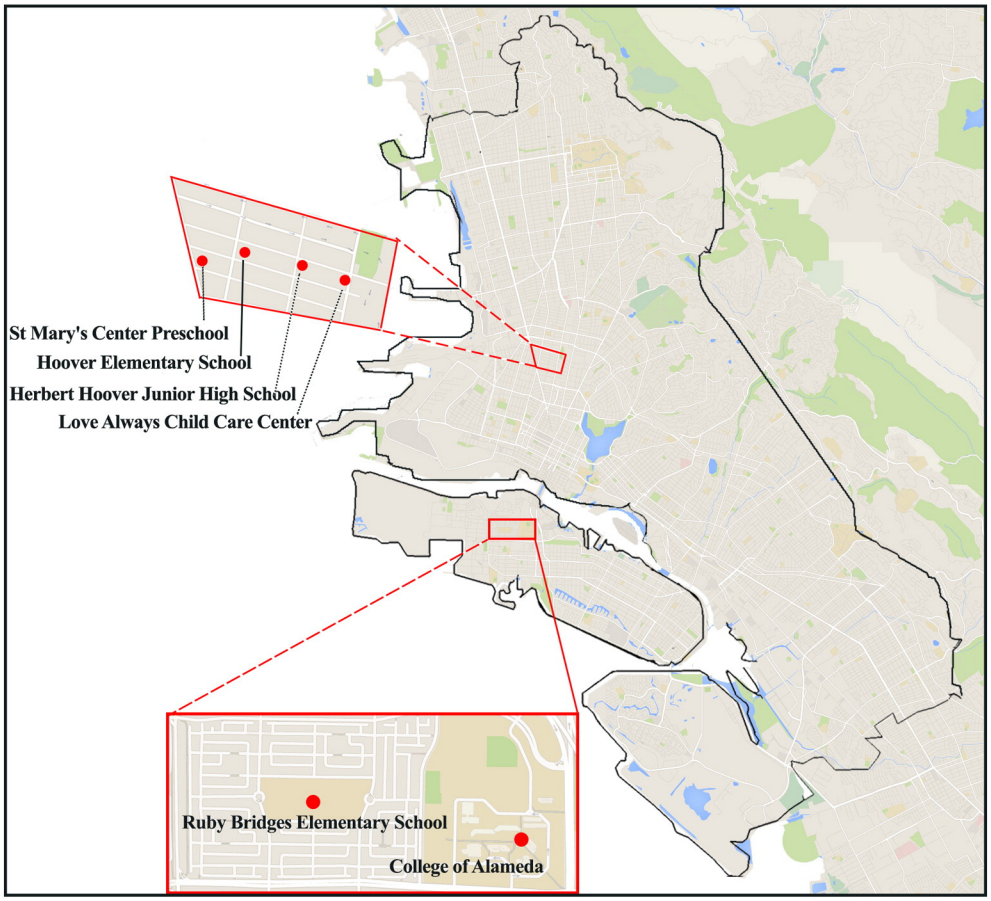

Fig. 14. Two subregions selected within Alameda County for local site-specific liquefaction hazard analysis.

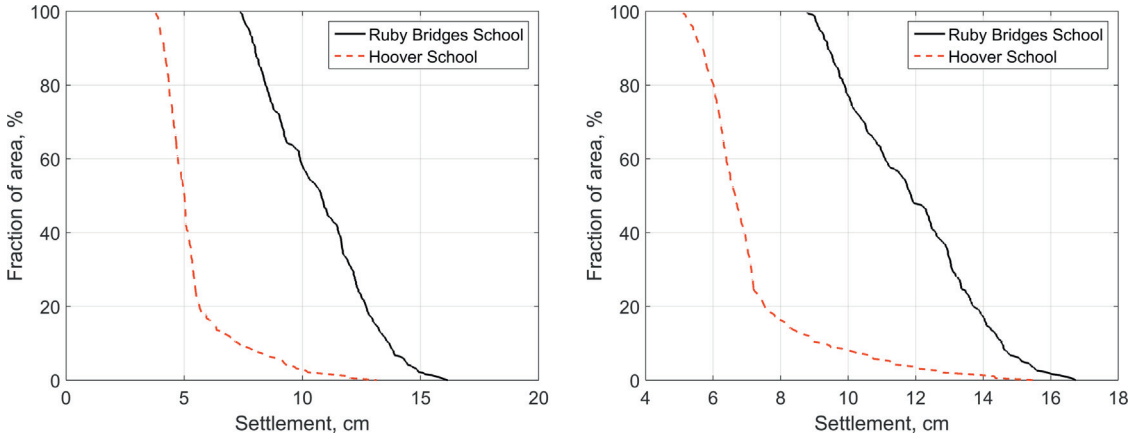

Fig. 15. Fraction of area exceeding a particular settlement for the Ruby Bridges School and Hoover School sites. (a) $M_w = 6.6$ earthquake (b) $M_w = 7.1$ earthquake.

high settlements. This region is mainly underlain by Merritt sand and Pleistocene fan deposits.

While the results show that the proposed framework predicts consistent liquefaction hazards for the entire region and for individual surficial geologic units, the multiscale random field models provide much more detailed information and are able account for spatial variability of the settlement within each geologic unit. This enables the assessment of local site-specific liquefaction hazards. To demonstrate this point, two local sites shown in Fig. 14 are picked from Alameda County. The first site is located on Alameda Island, consisting of Ruby Bridges Elementary School, the College of Alameda and a crowded residential area. This site will be referred to as the "Ruby Bridges School" site in the following analysis. The second local site, which includes schools and care centers such as St. Mary's Center Preschool, Hoover Elementary School, Herbert Hoover Junior High School and Love Always Child Care Center, will be referred to as the "Hoover School" site in the following analysis. The assessment is based on the same 1000 Monte Carlo simulations performed and used in previous cumulative frequency plots.

Fig. 15 shows the percentage of area predicted to exceed certain settlement values. It can be seen that 58% of the Ruby Bridges School site will suffer medium to extensive damage (settlement > 10 cm) for the $M_w = 6.6$ earthquake event, while the percentage is only 3% for the Hoover School site. For an $M_w = 7.1$ earthquake event, 75% of the Ruby Bridges School site and 9% of the Hoover School site will suffer medium to extensive damage.

Fig. 16 plots the percentage of area that will suffer medium to extensive damage and the corresponding probabilities for both $M_w = 6.6$ and $M_w = 7.1$ earthquake events for two sites. Again, the Ruby Bridges School site is expected to suffer more liquefaction-induced damage (quantified by the predicted settlements) than the Hoover School site. Such detailed information demonstrates the potential of the multiscale random field models for local site-specific liquefaction hazard analysis.

6. Conclusions

In this paper, a framework is developed that integrates the classical CPT-based liquefaction model with multiscale random field models and Monte Carlo simulations for the probabilistic and spatial assessment of liquefaction-induced settlements over a region and across scales. One critical advantage of the developed framework is its ability to consistently refine and provide settlement estimations across different scales, from regional and surficial geologic unit scale all the way to local site-specific scale. The developed framework is applied to the liquefaction hazard analysis of the Alameda County site in California and is demonstrated to be a valuable tool for multiscale regional liquefaction hazard analysis. In summary, it is found that

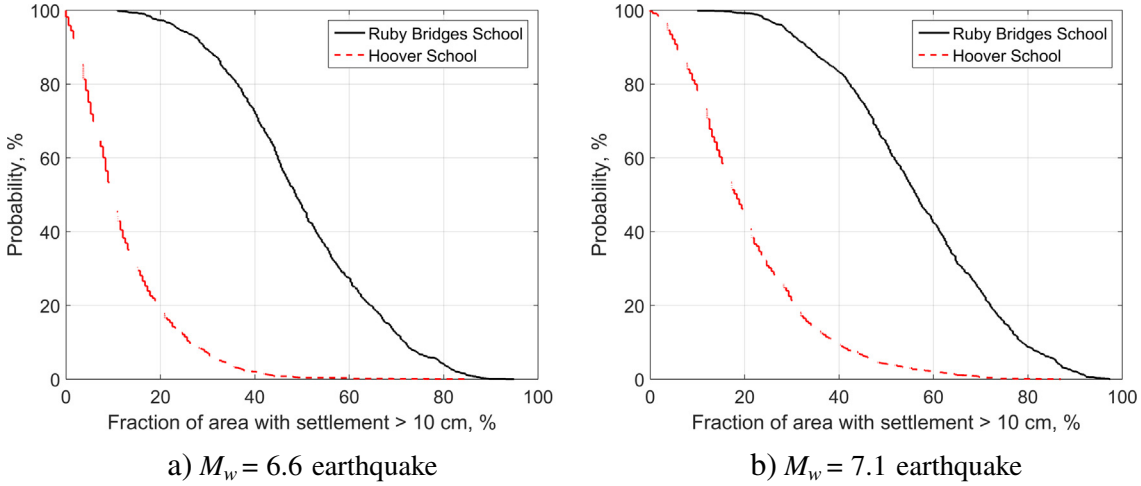

Fig. 16. Percentage of area that will suffer medium to extensive damage (settlement > 10 cm) vs. corresponding probabilities for the Ruby Bridges School and Hoover School sites. (a) $M_w = 6.6$ earthquake (b) $M_w = 7.1$ earthquake.

1. Quantitatively consistent liquefaction hazards over the entire studied region and within each surficial geologic unit are obtained when verified against existing analysis and knowledge of the studied region.
2. Spatial variability of soil properties within each geologic unit across different scales is captured, which provides a way to systematically refine and perform local site-specific liquefaction analysis while preserving the liquefaction hazard prediction at the regional scale.
3. The spatial structure of the predicted settlements inferred from available field data is shown to be relatively insensitive to the earthquake shaking intensity considered in this study ($M_w = 6.6$ and $M_w = 7.1$) and such inferred spatial structure is preserved during the random field modeling process.
4. In the Alameda County site, the artificial fill is the surficial geologic unit most susceptible to liquefaction hazard (48.2% and 57.7% of the area will exhibit medium to extensive damage for the $M_w = 6.6$ and $M_w = 7.1$ earthquake scenarios considered) followed by the Holocene alluvial fan deposits (the corresponding percentages are 7.4% and 13.2%).
5. Local site-specific analysis shows that the Ruby Bridges School site is expected to suffer more liquefaction-induced damage (quantified by the predicted settlements) than the Hoover School site.

Future work will fully incorporate uncertainties in the liquefaction settlement models, the input parameters, and the earthquake shaking intensities, and will explore the effect of these uncertainties in the regional liquefaction hazard analysis. Further validation of the estimated settlements from the proposed model against field observations from major earthquakes in this region (e.g., the 1989 Loma Prieta earthquake) is warranted.

Acknowledgment

Clemson University is acknowledged for the generous allotment of compute time on the Palmetto cluster. The authors thank Andrew Brownlow from Clemson University for proofreading and providing critical feedback to the paper. The expert reviews from three anonymous reviewers are also gratefully acknowledged.

References

Baise, L.G., Higgins, R.B., Brankman, C.M., 2006. Liquefaction hazard mapping — statistical and spatial characterization of susceptible units. J. Geotech. Geoenviron. 1320 (6), 705–715.
Baker, J.W., Faber, M.H., 2008. Liquefaction risk assessment using geostatistics to account for soil spatial variability. J. Geotech. Geoenviron. 1340 (1), 14–23.
Baker, J.W., Seifried, A., Andrade, J.E., Chen, Q., 2011. Characterization of random fields at multiple scales: an efficient conditional simulation procedure and applications in geomechanics. Appl. Stat. Probab. Civ. Eng. 347.
Bartlett, S.F., Youd, T.L., 1995. Empirical prediction of liquefaction-induced lateral spread. J. Geotech. Eng. 1210 (4), 316–329.
Bartlett, S.F., Gerber, T.M., Hinckley, D., 2007. Probabilistic liquefaction potential and liquefaction-induced ground failure maps for the urban Wasatch Front: phase IV. Technical Report Awards 07HQGR0021 and 07HQGR0024, Technical Report Submitted to the United States Geological Survey.
Cetin, K.O., Bilge, H.T., Wu, J., Kammerer, A.M., Seed, R.B., 2009a. Probabilistic models for cyclic straining of saturated clean sands. J. Geotech. Geoenviron. 1350 (3), 371–386.
Cetin, K.O., Bilge, H.T., Wu, J., Kammerer, A.M., Seed, R.B., 2009b. Probabilistic model for the assessment of cyclically induced reconsolidation (volumetric) settlements. J. Geotech. Geoenviron. 1350 (3), 387–398.
Chen, Q., Seifried, A., Andrade, J.E., Baker, J.W., 2012. Characterization of random fields and their impact on the mechanics of geosystems at multiple scales. Int. J. Numer. Anal. Methods Geomech. 360 (2), 140–165.
Chen, Q., Wang, C., Juang, C.H., 2015. CPT-based evaluation of liquefaction potential accounting for soil spatial variability at multiple scales. J. Geotech. Geoenviron. 04015077.
Cressie, N., 1985d. Fitting variogram models by weighted least squares. J. Int. Assoc. Math. Geol. 170 (5), 563–586.
Goovaerts, P., 1997. Geostatistics for Natural Resources Evaluation. Oxford University Press, New York.
Gringarten, E., Deutsch, C.V., 2001. Teacher's aide variogram interpretation and modeling. Math. Geol. 330 (4), 507–534.
Helley, E.J., Graymer, R.W., 1997. Quaternary geology of Alameda County, and parts of Contra Costa, Santa Clara, San Mateo, San Francisco, Stanislaus, and San Joaquin counties, California: a digital database. Technical Report 97–97, U.S. Geological Survey Open-File Report.
Hinckley, D.W., 2010. Liquefaction-induced ground displacement mapping for the Salt Lake Valley, Utah. The University of Utah (PhD thesis).
Holzer, T.L., Bennett, M.J., Noce, T.E., Padovani, A.C., Tinsley III, J.C., 2006. Liquefaction hazard mapping with LPI in the greater Oakland, California, area. Earthquake Spectra 220 (3), 693–708.
Isaaks, E.H., Srivastava, R.M., 1989. Applied Geostatistics. Oxford University Press, New York.
Ishihara, K., Yoshimine, M., 1992. Evaluation of settlements in sand deposits following liquefaction during earthquakes. Soils Found. 320 (1), 173–188.
Iwasaki, T., Tatsuoka, F., Tokida, K., Yasuda, S., 1978. A practical method for assessing soil liquefaction potential based on case studies at various sites in Japan. Proceedings 2nd International Conference on Microzonation, pp. 885–896.
Iwasaki, T., Tokida, K., Tatsuoka, F., Watanabe, S., Yasuda, S., Sato, H., 1982. Microzonation for soil liquefaction potential using simplified methods. Proceedings of the 3rd International Conference on Microzonation, Seattle vol. 3, pp. 1310–1330.
Juang, C.H., Li, D.K., Fang, S.Y., Liu, Z., Khor, E.H., 2008a. Simplified procedure for developing joint distribution of a_{max} and M_w for probabilistic liquefaction hazard analysis. J. Geotech. Geoenviron. 1340 (8), 1050–1058.
Juang, C.H., Liu, C.N., Chen, C.H., Hwang, J.H., Lu, C.C., 2008b. Calibration of liquefaction potential index: a re-visit focusing on a new CPTU model. Eng. Geol. 1020 (1), 19–30.
Juang, C.H., Ching, J., Wang, L., Khoshnevisan, S., Ku, C.S., 2013. Simplified procedure for estimation of liquefaction-induced settlement and site-specific probabilistic settlement exceedance curve using cone penetration test (CPT). Can. Geotech. J. 500 (10), 1055–1066.
Ku, C.S., Juang, C.H., Chang, C.W., Ching, J., 2012. Probabilistic version of the robertson and wride method for liquefaction evaluation: development and application. Can. Geotech. J. 490 (1), 27–44.
Lee, C.Y., 2007. Earthquake-induced settlements in saturated sandy soils. ARPN J. Eng. Appl. Sci. 20 (4), 6–13.
Lee, K.L., Albaisa, A., 1974. Earthquake induced settlements in saturated sands. J. Geotech. Eng. Div. ASCE 1000 (4), 387–406.
Lenz, J.A., Baise, L.G., 2007. Spatial variability of liquefaction potential in regional mapping using CPT and SPT data. Soil Dyn. Earthq. Eng. 270 (7), 690–702.
Liu, C.N., Chen, C.H., 2006. Mapping liquefaction potential considering spatial correlations of CPT measurements. J. Geotech. Geoenviron. 1320 (9), 1178–1187.
Lu, C.C., Hwang, J.H., Juang, C.H., Ku, C.S., Luo, Z., 2009. Framework for assessing probability of exceeding a specified liquefaction-induced settlement at a given site in a given exposure time. Eng. Geol. 1080 (1), 24–35.
Nagase, H., Ishihara, K., 1988. Liquefaction-induced compaction and settlement of sand during earthquakes. Soils Found. 280 (1), 65–76.
Papathanassiou, G., Pavlides, S., Ganas, A., 2005. The 2003 lefkada earthquake: Field observations and preliminary microzonation map based on liquefaction potential index for the town of Lefkada. Eng. Geol. 820 (1), 12–31.
Pradel, D., 1998. Procedure to evaluate earthquake-induced settlements in dry sandy soils. J. Geotech. Geoenviron. 1240 (4), 364–368.
Robertson, P.K., 2009. Performance based earthquake design using the CPT. Proc. IS-Tokyo, pp. 3–20.
Robertson, P.K., Wride, C.E., 1998. Evaluating cyclic liquefaction potential using the cone penetration test. Can. Geotech. J. 350 (3), 442–459.
Shamoto, Y., Zhang, J.M., Tokimatsu, K., 1998. Methods for evaluating residual post-liquefaction ground settlement and horizontal displacement. Soils Found. 38, 69–84.
Sonmez, H., 2003. Modification of the liquefaction potential index and liquefaction susceptibility mapping for a liquefaction-prone area (Inegol, Turkey). Environ. Geol. 440 (7), 862–871.
Sonmez, H., Gokceoglu, C., 2005. A liquefaction severity index suggested for engineering practice. Environ. Geol. 480 (1), 81–91.
Sowers, J.M., Richard, C.M., 2010. Creek & Watershed Map of Oakland and Berkeley. Oakland Museum of California.
Thompson, E.M., Baise, L.G., Kayen, R.E., 2007. Spatial correlation of shear-wave velocity in the San Francisco Bay Area sediments. Soil Dyn. Earthq. Eng. 270 (2), 144–152.
Tokimatsu, K., Seed, H.B., 1984. Simplified procedures for the evaluation of settlements in clean sands. Technical Report CB/EERC-84/16. Earthquake Engineering Research Center, University of California.
Tokimatsu, K., Seed, H.B., 1987. Evaluation of settlements in sands due to earthquake shaking. J. Geotech. Eng. 1130 (8), 861–878.
Toprak, S., Holzer, T.L., 2003. Liquefaction potential index: field assessment. J. Geotech. Geoenviron. 1290 (4), 315–322.
Trask, P., Rolston, J., 1951. Engineering geology of San Francisco Bay, California. Geol. Soc. Am. Bull. 620 (9), 1079–1110.
Tsukamoto, Y., Ishihara, K., 2010. Analysis on settlement of soil deposits following liquefaction during earthquakes. Soils Found. 500 (3), 399–411.
Tsukamoto, Y., Ishihara, K., Sawada, S., 2004. Settlement of silty sand deposits following liquefaction during earthquakes. Soils Found. 440 (5), 135–148.
Ueng, T., Wu, C., Cheng, H., Chen, C., 2010. Settlements of saturated clean sand deposits in shaking table tests. Soil Dyn. Earthq. Eng. 300 (1), 50–60.
USGS, 2014. U.S. Geological Survey National Seismic Hazard Maps. http://earthquake.usgs.gov/hazards/products/conterminous/2014/data/.
USGS, 2015. U.S. Geological Survey Hazards Program CPT database. http://earthquake.usgs.gov/research/cpt/.
Valverde-Palacios, I., Vidal, F., Valverde-Espinosa, I., Martn-Morales, M., 2014. Simplified empirical method for predicting earthquake-induced settlements and its application to a large area in spain. Eng. Geol. 181, 58–70.
van Ballegooy, S., Wentz, F., Boulanger, R.W., 2015. Evaluation of CPT-based liquefaction procedures at regional scale. Soil Dyn. Earthq. Eng. 79, 315–334.
Vivek, B., Raychowdhury, P., 2014. Probabilistic and spatial liquefaction analysis using CPT data: a case study for Alameda County site. Nat. Hazards 710 (3), 1715–1732.

WGCEP, 2003. Earthquake probabilities in the San Francisco Bay region 2002–2031: a summary of findings. Technical Report U.S. Geological Survey Open-file Report 03–214. United States Geological Survey.

Wu, J., Seed, R.B., 2004. Estimation of liquefaction-induced ground settlement (case studies). Proceedings of the 5th International Conference on Case Histories in Geotechnical Engineering number 6. Springer.

Yoshimine, M., Nishizaki, H., Amano, K., Hosono, Y., 2006. Flow deformation of liquefied sand under constant shear load and its application to analysis of flow slide of infinite slope. Soil Dyn. Earthq. Eng. 260 (2), 253–264.

Youd, T.L., Idriss, I.M., Andrus, R.D., Arango, I., Castro, G., Christian, J., Dobry, R., Finn, D.W.L., Harder Jr., L.F., Hynes, M.E., Ishihara, K., Koester, J., Liao, S., Marcuson, W.I., Martin, G., Mitchell, J., Moriwaki, Y., Power, M., Robertson, P., Seed, R., Stokoe, K.I., 2001. Liquefaction resistance of soils: summary report from the 1996 NCEER and 1998 NCEER/NSF workshops on evaluation of liquefaction resistance of soils. J. Geotech. Geoenviron. 1270 (4), 297–313.

Youd, T.L., Hansen, C.M., Bartlett, S.F., 2002. Revised multilinear regression equations for prediction of lateral spread displacement. J. Geotech. Geoenviron. 1280 (12), 1007–1017.

Zhang, G., Robertson, P.K., Brachman, R.W.I., 2002. Estimating liquefaction-induced ground settlements from CPT for level ground. Can. Geotech. J. 390 (5), 1168–1180.